

# Assessment of High-Temperature Hydrogen Attack Using Advanced Ultrasonic Array Techniques

by M.G. Lozev<sup>\*††</sup>, G.A. Neau<sup>†</sup>, L. Yu<sup>‡</sup>, T.J. Eason<sup>‡</sup>, S.E. Orwig<sup>††</sup>, R.C. Collins<sup>‡</sup>, P.K. Mammen<sup>††</sup>, F. Reverdy<sup>†</sup>, S. Lonne<sup>§</sup>, C. Wassink<sup>†</sup>, H. Cence<sup>¶</sup>, and J. Chew<sup>‡</sup>

## ABSTRACT

The ability to measure early-stage high-temperature hydrogen attack (HTHA) has been improved by the use of optimized ultrasonic array probes and techniques. First, ultrasonic modeling and simulations were performed to design a set of array probes. The data was then collected using phased array ultrasonic testing (PAUT) and full matrix capture (FMC) techniques. Damage visualization, characterization, and sizing was completed with PAUT, total focusing method (TFM), and adaptive total focusing method (ATFM) advanced algorithms. The detection and sizing capabilities were initially validated on steel calibration samples with micromachined defects and synthetic HTHA damage. Vessels with suspected HTHA damage were removed from service, inspected with multiple array techniques, and then destructively evaluated for a results comparison with metallographic images. This study concluded that the FMC/TFM/ATFM techniques and algorithms improve detectability, characterization, and sizing of early-stage HTHA damage as compared to PAUT.

**KEYWORDS:** high-temperature hydrogen attack, phased array ultrasonic testing, full matrix capture, total focusing method, adaptive total focusing method

*Materials Evaluation* 78 (11): 1223–1238  
<https://doi.org/10.32548/2020.me-04183>  
 ©2020 American Society for Nondestructive Testing

\* nde4zero LLC, Chapel Hill, NC, USA; mlozev@nde4zero.com  
 † Eddyfi Technologies, 3425 Rue Pierre-Arduin, Quebec, QC G1P 0B3, Canada  
 ‡ bp, 150 W. Warrenville Rd., Naperville, IL 60563 USA  
 § Extende, 14 Avenue Carnot, 91300 Massy, France  
 ¶ Ekoscan, 3 Rue Desire Gillot, 71100 Saint-Remy, France  
 †† formerly with bp, 150 W. Warrenville Rd., Naperville, IL 60563 USA

## Introduction

High-temperature hydrogen attack (HTHA) is a localized complex damage phenomenon. HTHA occurs in welds, weld heat-affected zones (HAZs), and base materials in carbon and low-alloy steels exposed to a high partial pressure of hydrogen at elevated temperatures. HTHA is possible in hydrocarbon-processing units, hydrogen-producing units, synthetic gas units, ammonia plants under dry conditions, and in high-pressure boiler tubes in a wet environment. HTHA typically initiates near to the internal diameter (ID) surface and the appearance includes:

- decarburization: surface and internal
- volumetric-like damage: voids (methane bubbles), linking voids, disoriented microcracking (fissures)
- blister-like damage: bubbles accumulating in steel laminations near and parallel to ID surface
- crack-like damage: vertical or inclined cracks

Detection, characterization, and sizing of HTHA is a challenging inspection task due to the complexity of the damage. Past editions of API RP 941 recommend many manual ultrasonic techniques developed in the 1980s and 1990s (API 2016). These techniques have limitations, including operator variability. Wang investigated and improved several historical techniques such as ultrasonic backscattering, frequency analysis, velocity ratio, and high-frequency shear wave (Wang 1999). The advanced ultrasonic backscattering technique (AUBT) can detect HTHA damage at a depth of 10% to 20% wall thickness (Kallenberg and Munsterman 2002). Time of flight diffraction (TOFD) is an emerging screening technique for the inspection of two-side access welds (API 2016; ASME 2019). TOFD cannot detect HTHA damage at a depth of 10% to 12% wall thickness due to internal and external diameter “dead zone” limitations. TOFD can detect simulated HTHA in the weld HAZ, but with wavelength and imaging limitations, it cannot distinguish HTHA microcracking damage from acceptable inclusions, slag, and porosity (Birring et al. 2005). Regardless, TOFD has been applied for HTHA inspection applications (Krynicky et al. 2006). The PAUT technique has been used for HTHA detection, characterization, and sizing (Birring et al. 2005). Noncollinear wave mixing of ultrasonic waves has been applied to a test sample extracted from a retired pressure vessel exposed to hydrogen

(McGovern et al. 2017). First, FMC/TFM and ATFM ultrasonic techniques were applied for enhanced HTHA detection, characterization, and sizing; next, a comparison of PAUT and FMC capabilities to detect HTHA damage was confirmed by metallography; then, TOFD limitations to distinguish HTHA from metallurgical imperfections was confirmed; and lastly, novel principles for progressive validation and qualification using specimens extracted from service were proposed (Lozev et al. 2017). A UK HSE report reviews historical and new ultrasonic techniques for HTHA inspection, describes limitations of the techniques, and addresses ongoing efforts to codify the new techniques, evaluate inspection effectiveness, and provide training (Nageswaran 2018). PAUT, FMC/TFM, and TOFD techniques have been used for HTHA field inspections (Reverdy et al. 2018; Johnson et al. 2019; Le Nevé et al. 2019).

**Approach**

This paper presents an approach for optimizing and evaluating the capabilities of codified ultrasonic array techniques for improved detection, characterization, and sizing of early-stage HTHA in refining equipment. TOFD was not selected for this study because the characterization concerns and dead-zone limitations prohibit the detection of early-stage HTHA damage developed near the ID surface. A short overview of PAUT and FMC/TFM techniques are presented. Ultrasonic modeling and simulation tools were used to design and optimize a set of linear and matrix array probes tailored for HTHA inspection. The predicted capabilities of the probes to detect and size HTHA damage smaller than 1 mm (microscopic damage), utilized with PAUT sectorial scanning and FMC/TFM/ATFM longitudinal to longitudinal (LL) and transverse to transverse (TT) direct path techniques, were validated. Samples with micromachined defects, synthetic HTHA, and real HTHA damage were used. The results of the ultrasonic array techniques were compared with metallographic images and measurements.

**Ultrasonic Array Techniques**

**General**

Both PAUT and FMC/TFM use an array transducer with multiple piezocomposite elements in a common housing. The aperture is chosen such that the inspection volume is placed in the near field of the sound beam.

PAUT is a beamforming (BF) technique often used in the field. The fundamental physics and unique characteristics of PAUT are described in the literature (Schmerr Jr. 2015). Compared to conventional ultrasonic techniques with fixed beam angles, PAUT offers detection and sizing advantages, because it acquires more data by covering a large range of angles (sweep), focusing the beam, and enhancing the imaging with a sectorial (S) scan.

The mathematics for postprocessing of FMC data using the TFM algorithm, as an expansion of the synthetic aperture focusing technique (SAFT) and as an alternative approach to PAUT imaging methodologies, were introduced by Holmes et al. (2004). At the FMC acquisition step, the complete set of time domain signals (waveforms or A-scans) from every transmitter–receiver element pair is collected and buffered (stored) as a matrix data structure. The transmission and reception are performed sequentially, and the process is repeated until all elements of the array have been used. After data collection, the TFM postprocessing algorithm generates a color image in which the beam has been focused at the reception on every grid point within the region of interest (RoI). The TFM computational algorithm provides clear imaging and allows resolution below the one-half wavelength limit for PAUT and TOFD. A paper by Wilcox (2013) examines the ways in which FMC/TFM can be exploited to improve ultrasonic examinations. The theoretical background of the ATFM imaging method and applications of an ultrasonic array probe equipped with a conformable elastomer wedge were discussed by Robert et al. (2016).

PAUT and FMC/TFM techniques have been codified in Section 5 of the ASME Code and API RP 941 Addendum 1 (ASME 2019; API 2020).

**TABLE 1**  
Specifications summary for the probes: central frequency, aperture, and near field at –6 dB

Probe central frequency (MHz)	Aperture (mm <sup>2</sup> )		Normal beam L-wave, no wedge/thermoplastic 1 mm wedge (near field, mm)		Normal beam L-wave, 23/20 mm height Rexolite wedge (near field, mm)		Normal beam L-wave, 23/20 mm height water wedge (near field, mm)		Angle beam S/T-wave, SW55° 45/29/14 mm height Rexolite wedge (near field/depth, mm)		Angle beam S/T-wave, SW55° 45/29/14 mm height water wedge (near field/depth, mm)	
	Linear (1 × 64 elements)	Matrix (4 × 16 elements)	Linear (1 × 64 elements)	Matrix (4 × 16 elements)	Linear (1 × 64 elements)	Matrix (4 × 16 elements)	Linear (1 × 64 elements)	Matrix (4 × 16 elements)	Linear (1 × 64 elements)	Matrix (4 × 16 elements)	Linear (1 × 64 elements)	Matrix (4 × 16 elements)
5	320	160	298	96	287	89	290	90	277/162	89/53	206/119	70/41
7.5	250	130	311	132	297	120	307	122	285/167	119/70	211/122	91/53
10	150	60	198	65	190	62	194	62	186/109	60/36	145/83	50/29

### Design and Optimization of Array Probes

The design of the probes and optimization of the inspection procedures were based on a two-step approach applying semi-analytical tools and an advanced software package for processing, imaging, and simulations (Lozev and Spencer 2005; Calmon et al. 2018). The array aperture was limited to 64 elements in both linear (1 × 64) and matrix (4 × 16) arrangements with a probe frequency ranging from 5 to 10 MHz.

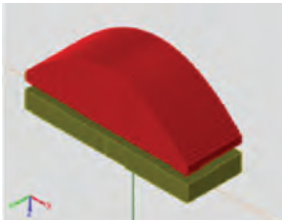
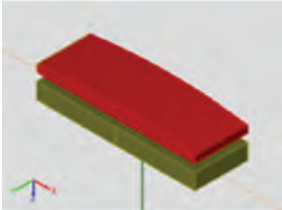
In the first optimization step, called modeling, an unfocused (natural) beam profile for each probe was calculated, visualized, and used to determine the near field. Next, a profile for each beam focused at a specific depth was calculated and beam cross sections were visualized. All beam calculations were performed for the following combinations of wedges: (1) normal beam with no wedge (hard face probe); (2) normal beam with solid, 1 mm thick thermoplastic wedge; (3) normal beam with solid, 20 to 23 mm thick Rexolite wedge; (4) normal beam with conformable (flexible) elastomer wedge filled with water, with a height of 20 mm; (5) angle beam with solid Rexolite wedge, height 14, 29, and 45 mm; and (6) angle beam with conformable (flexible) elastomer wedge filled with water, with a height of 14, 29, and 45 mm. The natural focal spot was calculated and specified in three dimensions at -3, -6, and -9 dB levels from peak

amplitude. The central frequency, aperture, and near field for the developed set of linear and matrix probes are shown in Table 1. The near field represents the optimum thickness range for PAUT and FMC/TFM inspections in carbon and low-alloy steels. This information assists operators in selecting the right probe for performing HTHA inspection only in the near field and to improve detection and characterization capabilities.



The 3D-focused beam at selected depths was visualized and used to calculate the focal length (spot) and the beam size in two planes for both normal and angle beam probes. Focal spot sizes were then calculated for each probe and combinations of wedges at a 25 mm depth, and at the end of the near field as shown in Table 2. Focal spot sizes were calculated at -3, -6, and -9 dB. This specification information assists operators in selecting the right probe for performing HTHA inspection with a minimum spot size and to improve characterization and sizing capabilities.

In the second optimization step, a simulation was used to visualize the interaction of the beam from each probe and microscopic defects virtually implanted in a 25 mm thick double-V bevel carbon steel weld. The objective of the simulation was to define the capabilities of the probes utilized with both techniques to detect and size defects smaller than 1 mm. PAUT sectorial scan and FMC/TFM LL and TT techniques

**TABLE 2A**  
Beam sizes of 10 MHz, 64 elements, linear array probe at depth 25 and 124 mm: longitudinal wave, no wedge

Contact – no wedge – focusing	3D focal spot sizes at -3 dB, -6 dB, and -9 dB			Focal depth (mm)	Associated depth at 55° in carbon steel (mm)	
	X (mm)	Y (mm)	Z (mm)			
25 mm depth	-3 dB	0.4		4.4	25	
			1.9	4.4		
	-6 dB	0.7		6.2		
			3.6	6.2		
-9 dB	0.9		7.6			
		5.3	7.6			
Contact – no wedge – focusing near field limit distance (198 mm)	3D focal spot sizes at -3 dB, -6 dB, and -9 dB			Focal depth (mm)	Associated depth at 55° in carbon steel (mm)	
	X (mm)	Y (mm)	Z (mm)			
198 mm	-3 dB	5.2		98.2	124	
			6.9	85.7		
	-6 dB	7.7		132.2		
			9.9	130.2		
-9 dB	9.5		167.7			
		12.7	167.7			

**TABLE 2B**  
 Beam sizes of 10 MHz, 64 elements, linear array probe at depth 25 and 67 mm: shear wave, Rexolite wedge

	3D focal spot sizes at -3 dB, -6 dB, and -9 dB				Focal distance (mm)	Associated depth at 55° in carbon steel (mm)	
		X (mm)	Y (mm)	Z (mm)			
Contact – Rexolite wedge SW55° – focusing 25 mm depth	-3 dB	0.6		15.5	41.5	24.26	
			1.9	15.9			
	-6 dB	1.1		22.5			
			2.9	23.1			
	-9 dB	1.4		28.6			
			3.9	29.1			
Contact – Rexolite wedge SW55° – focusing near field limit distance (277 mm)	-3 dB	1.7		82.8	114	66.64	
			4	82.8			
	-6 dB	8.2		181.9			
			5.9	130.9			
	-9 dB	10.2		227.3			
			7.5	218			

were simulated and results were visualized in standard A-, B-, C-, D-, and S-views. The maximum amplitude difference in decibels with respect to a 2 × 10 mm (diameter × length) reference side-drilled hole (SDH) was recorded for the following defects:

- one cluster of six SDHs with diameters of 0.4 mm in HAZ at ID surface, simulating in-service HTHA volumetric damage (clustered linking voids and disoriented microcracking)

- two notches with 0.4 mm height at top surface and bottom surface, simulating in-service HTHA crack-like damage
- three lack of fusion (LOF) defects with heights of 0.4 mm along the weld lines (top, middle, and bottom) simulating fabrication defects (metallurgical discontinuities)

Examples of beam interaction with simulated clusters of volumetric damage using a 10 MHz linear probe with solid Rexolite wedges are shown in Figure 1.

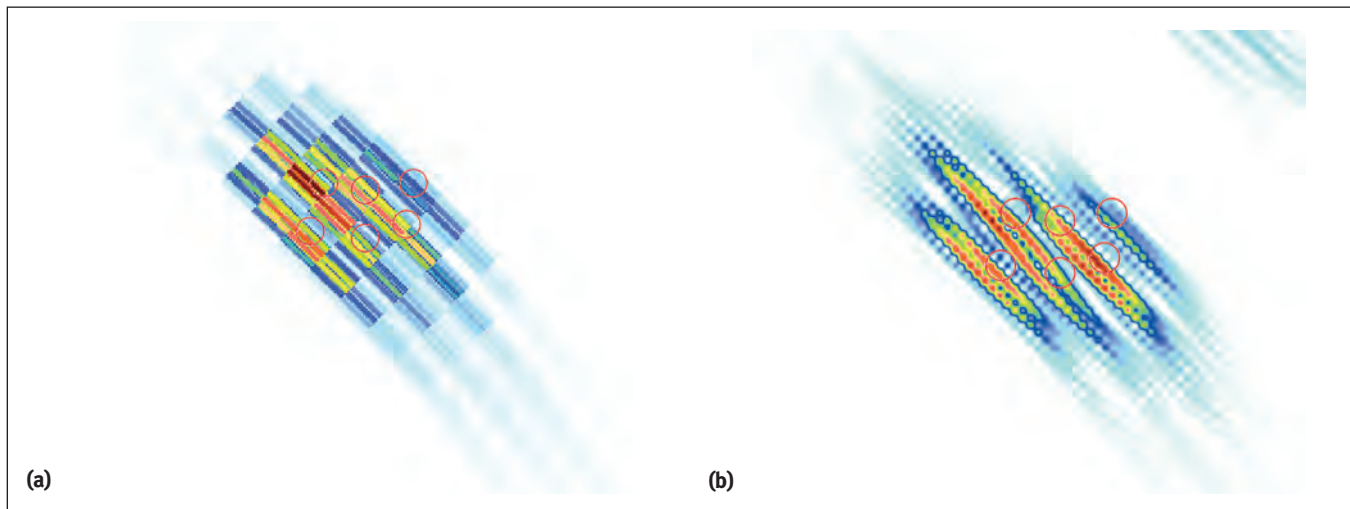


Figure 1. 10 MHz shear wave beam interactions with a cluster of six SDHs: (a) PAUT; (b) FMC/TFM TT.



**TABLE 3**  
**Vessel material and process parameters**

Vessel	Unit	Material	Wall thickness (mm)	H <sub>2</sub> partial pressure (MPa)	Fluid temperature in (°C)	Fluid temperature out (°C)	Years in service
Depentanizer reboiler channel	Hydrotreater	C – 0.5 Mo	14	1.5	400	385	53
Zinc oxide drum	Hydrogen plant	C – 0.5 Mo	34	2.1	385	370	45

Simulations predicted that HTHA microdamage is detectable only in the higher end of the investigated frequency range. Simulation results predicted that both PAUT and FMC/TFM 10 MHz techniques can detect all microscopic defects; however, the TFM/FMC technique was more precise at sizing micro indications, including the height and separation in SDH clusters. It was demonstrated that HTHA indications detected with a higher frequency will be missing at the lower frequency range. Large macro HTHA damage may be detected and visualized using 5 MHz techniques, but the number of indications will be limited. Regardless, the accuracy of sizing is dependent on the wavelength and array aperture.

## Capabilities Validation

### Samples Selection and Preparation

The capabilities of ultrasonic array techniques were validated and qualified in three steps using a library of samples with (1) machined defects, (2) synthetic HTHA damage, and (3) samples removed from service during progressive validation and qualification.

Two carbon steel bars with micromachined defects were employed for the first validation step and the initial assessment of the techniques. Using micromachined defect samples allowed a comparison of ultrasonic findings with as-built dimensions without cutting the samples. Thirty-six micro SDHs mimicking volumetric damage were machined and grouped into three clusters. The height (diameter) of the SDHs varied from 0.18 to 0.40 mm, the vertical separations varied from 0.07 to 0.90 mm, and the overall cluster dimensions varied from 0.7 (length) × 1.3 (height) mm to 1.7 (length) × 3.0 (height) mm. Blister-like damage was represented by six shallow micro flat bottom holes (FBHs) with the diameter and height (depth) of less than 1 mm. Crack-like indications were imitated by two stepwise defects with the height and length of the steps at less than 1 mm.

Two carbon steel blocks with synthetic HTHA damage were used in the second step. The initial block material was baseline tested using a 15 MHz, 64-element linear probe with the FMC/TFM LL path technique. The baseline inspection

verified that the material was free of micro/macro inclusions and laminations. Introducing synthetic damage in the validation samples permitted controlling the stage and spread of HTHA damage with less complexity. The samples were critical for optimizing the characterization capabilities of the techniques.

Samples from two vessels removed from service were investigated in the third step. The samples with in service-induced damage represent the unique HTHA morphology and localized manifestation at different stages and spreading across the components. These samples are very rare and difficult to collect. The samples with real HTHA damage were the most reliable source for assessing the capabilities of the techniques before recommending widespread deployment in the field. Materials and process parameters of the vessels are presented in Table 3.

Ten sections of a channel and eight large areas of a drum were selected for inspection. Multiple samples containing indications for potential HTHA damage were removed for destructive metallographic verification of the ultrasonic array findings. Precise electrical discharge machining cuts and progressive grinding were used to validate the height and length extremes of the selected indications. Computed tomography (CT) was used to verify the location and sizes of HTHA damage below the polished surface in the remnants of selected metallographic mounts.

### Experimental Setups and Calibrations

A battery-powered, 64-channel ultrasonic instrument with parallel architecture was used. The instrument was integrated with fully and semi-automated scanners for multiple array probe designs with solid wedges (Rexolite and thermoplastic) and conformable (flexible) elastomer wedges filled with water. Normal-beam L-wave array probes were used for inspection and damage verification on base material with all wedge designs, and on welds without removing the reinforcement (crown) with flexible wedge designs. Angle beam shear wave (SW) array probes were used for weld inspection and base material damage verification. The setups for fully automated PAUT and FMC/TFM of the vessels are shown in Figure 2.

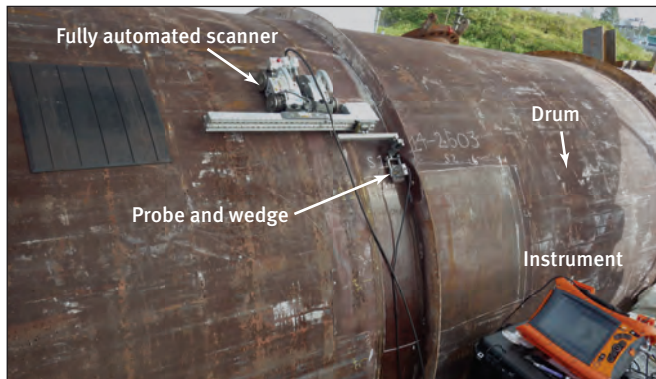


Figure 2. Setup for fully automated PAUT and FMC/TFM.

The distance validation, sensitivity, and amplitude fidelity check per Section 5 of the ASME Code (ASME 2019) with and without time-corrected gain (TCG) was completed on a NAVSHIPS test block (AISI 1018 mild/low-carbon steel), ASTM PAUT blocks, and 1.2 mm diameter SDHs fabricated in the test components.

#### Data Collection and Analysis

Line and/or raster scanning for data collection and typical C- (top view), B- (T- or end view), and D- (side or front view) scans were used for localization and sizing of HTHA damage. In addition, PAUT S-scan view and single-plane TFM view were used for sizing verification. Data collection scans were performed at multiple frequencies and 12 dB above the reference gain.

A general rule of thumb for this study was that HTHA damage must be larger than one-half of the wavelength ( $\lambda$ ) to be detected and separated using at least one of the selected array techniques. PAUT sensitivity and resolution were limited to half wavelength (for carbon steel, 10 MHz SW: 0.16 mm/160  $\mu\text{m}$ ) and the focal spot size. Classical TFM sensitivity and resolution were limited to one-tenth of the wavelength and ROI grid's density (for carbon steel, 10 MHz SW, 497  $\times$  497 grid points in 25  $\times$  25 mm ROI: 0.016 mm/16  $\mu\text{m}$ ). The theoretical pixel size limit of 0.28 $\lambda$  ( $\sim\lambda/3.6$ ) was used for calculations of pixel size and resolution (wavelength ratio) for selected ROIs employed in this study.

The first steps of the analysis were (1) detection to identify the presence or absence of HTHA damage or metallurgical imperfections, and (2) characterization. The analysis was performed at the reference gain or with a reduced 3 to 6 dB gain. When a mix of metallurgical imperfections and micro/macro HTHA damage was present in both techniques, 3D visualization and segmentation were used to improve the characterization process and differentiate HTHA damage from metallurgical imperfections.

The second step of the analysis was sizing. The tip diffraction technique was used for crack-like and blister-like damage height sizing when the tip was detected and imaged. The 6 dB or 3 dB drop imaging techniques were used for crack-like,

blister-like, and volumetric damage height sizing when the tip was not detected. The same techniques were used for length sizing.

The best results were achieved following these rules:

- Use the highest practical frequency for a specific base material, weld, and wall thickness.
- Work in the near field (aperture and frequency dependent).
- Use the smallest beam spot for PAUT (aperture and frequency dependent).
- Use the highest density grid in ROI for FMC/TFM/ATFM (ROI size and number of pixels dependent).

#### Investigation of Samples with Machined Defects

The capabilities of the PAUT sectorial scanning and FMC/TFM/ATFM (LL and TT paths) techniques were initially validated using samples with micromachined defects with known sizes and separations.

The 7.5 and 10 MHz FMC/TFM TT techniques detected all the micromachined defects. Only the 10 MHz FMC/TFM TT technique separated all the micro SDHs grouped in the clusters. A grid density of 256  $\times$  256 pixels for two ROIs (25  $\times$  25 mm and 5  $\times$  5 mm) were investigated. Examples of TFM imaging from two directions (skew 90 and 270) of the cluster with the smallest micro SDHs are shown in Figure 3. The cluster consists of the six SDHs, with overall cluster dimensions of 0.7 (length)  $\times$  1.3 (height) mm. The height (diameter) of each SDH is 0.18  $\pm$  0.06 mm, and the vertical separations of the SDHs vary from 0.07 to 0.90 mm.

A comprehensive imaging analysis of the clusters and each SDH was performed for two ROIs. The clusters, simulating microdefects concentrated in the vertical-extend range from

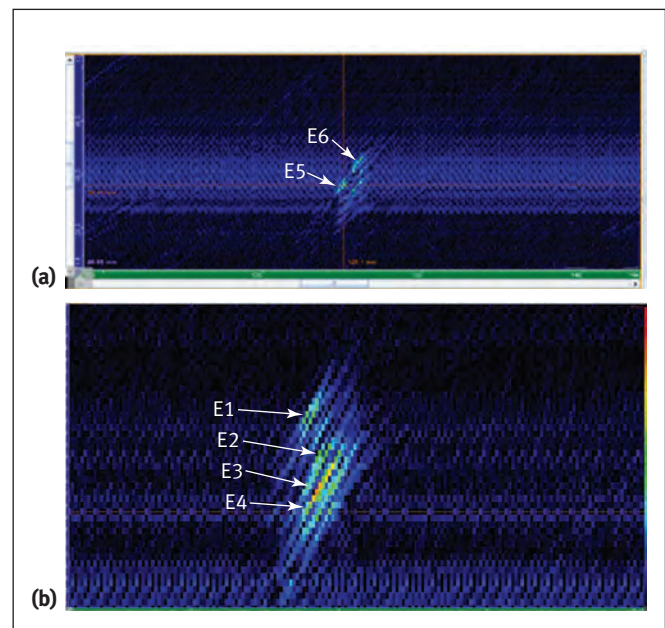


Figure 3. 10 MHz TFM TT imaging of clustered micromachined defects: (a) skew 90; (b) skew 270.

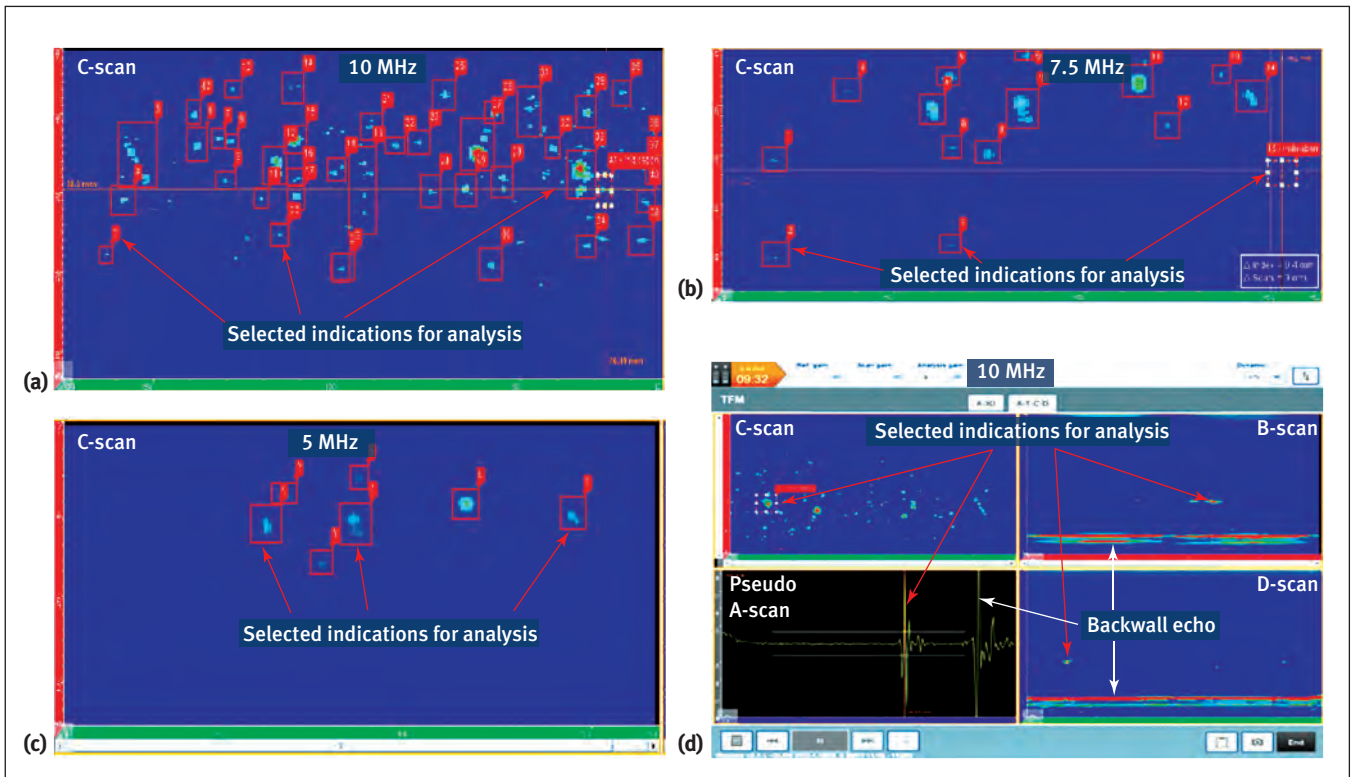


Figure 4. FMC/TFM LL imaging of damage block: (a) 10 MHz projected C-scan; (b) 7.5 MHz projected C-scan; (c) 5 MHz projected C-scan; (d) 10 MHz split screen imaging of selected indication showing projected C-scan, single-plane B-scan, single-plane D-scan, and pseudo A-scan.

1 to 3 mm, were oversized with up to 20% error when a  $5 \times 5$  mm ROI was used, and up to 50% when a  $25 \times 25$  mm ROI was used. Single SDHs, simulating microdefects in the range of 0.18 to 0.40 mm ( $180$  to  $400 \mu\text{m}$ )  $\pm 0.06$  mm ( $60 \mu\text{m}$ ) were oversized in an average with 20% to 50% error when a  $5 \times 5$  mm ROI was used and in an average with 50% to 100% when a  $25 \times 25$  mm ROI was used. The height measurements using a  $5 \times 5$  mm ROI were very accurate as the spatial resolution was improved by the ROI pixel resolution; the height measurements using a  $25 \times 25$  mm ROI were still acceptable considering the microscopic defect size. The errors for separation measurements were less than 20% using a  $5 \times 5$  mm ROI and less than 50% using a  $25 \times 25$  mm ROI. The vertical separation measurements using both ROIs are very accurate for the range of 0.4 to 1.1 mm separation.

A good agreement between the simulation predictions and TFM experimental sizing and separation measurements was demonstrated using samples with micromachined defects with known sizes and separations.

#### Investigation of Samples with Synthetic HTHA Damage

In the second investigation step, the capabilities of PAUT sectorial scanning and the FMC/TFM/ATFM (LL and TT paths) techniques were validated using samples containing synthetic HTHA damage with controlled distribution and morphology.

The blocks were inspected using the array techniques before and after the synthetic HTHA damage was introduced. The best detection results were obtained using 10 MHz linear and matrix probes, and the FMC/TFM technique in LL path/mode. The 10 MHz FMC/TFM projected C-scan is shown in Figure 4a. More than 100 micro and macro indications were identified (shown in boxes). Only 30% of the indications were observed on the projected C-scan created by using a lower-frequency 7.5 MHz linear array probe (Figure 4b), and only 10% of the indications were detected when using a 5 MHz linear array probe (Figure 4c). These images demonstrated the decrease in detectability and resolution at a lower frequency and the potential increase of the sizing error.

Figure 4d illustrates a split screen analysis using a C-scan, a single-plane B- and D-scan, and a pseudo A-scan. One large indication of HTHA microdamage was selected for analysis and boxed in the projected top view image shown in the top-left corner of Figure 4d. The red color of the image indication is a sign of strong reflected and diffracted signals from the damage and was confirmed by pseudo A-scan (Figure 4d, bottom left). The same indication is marked with a crossing of X/Y measuring cursors in the single-plane side view (Figure 4d, top right) and front view (Figure 4d, bottom right). This indication is relatively near to the hot surface of the block,



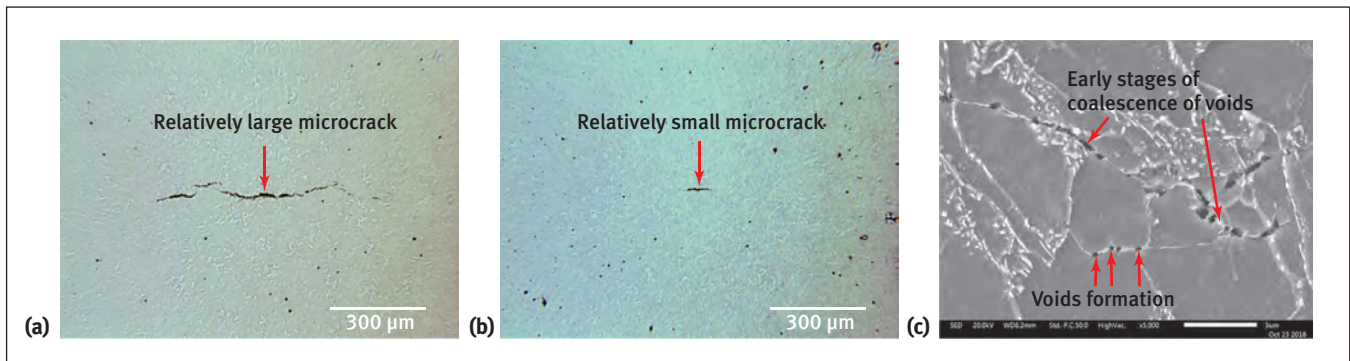


**Figure 5. Optical microscopy and SEM imaging of synthetic HTHA damage: (a) fissures forming relatively large microcrack indicative of HTHA damage (~100 $\times$ , as polished); (b) fissures forming small microcrack indicative of HTHA damage (~100 $\times$ , as polished); (c) damage feature showing severe dissolution of grain boundaries, grain boundary single void formation, and early stages of coalescence of voids in the periphery of the main feature, indicative of HTHA volumetric damage (~5000 $\times$ , as polished).**

which was exposed to hydrogen. The estimated length of the indication in TFM front view was ~0.7 mm (~700  $\mu\text{m}$ ). Multiple small indications of HTHA volumetric damage were observed in both planes and are represented by light blue dots.

The presence and the length of a ~0.7 mm (~700  $\mu\text{m}$ ) indication was validated at low magnification using optical microscopy (Figure 5a). Optical microscopy at a lower magnification (shown in Figure 5b) displayed a smaller ~0.1 mm (~100  $\mu\text{m}$ ) fissure-forming isolated microcrack below the larger microcrack. The separation between these microcracks is larger than the pixel size, and microcracks can be visualized as isolated indications. Scanning electron microscopy (SEM) at a higher magnification revealed damage features ~0.01 mm (~10  $\mu\text{m}$ ) showing severe dissolution of grain boundaries, some early stages of single submicron void formation, and some early stages of coalescence of voids in the periphery of the main feature (Figure 5c). Submicron void formations are not detectable by any of the techniques evaluated in this study. No evidence was obtained to verify that any of the investigated techniques were capable of detecting linking voids at one grain boundary or clustered linking voids in a small volume. If limited fissures start forming small microcracks in the clustered linking voids along 5 to 10 damaged grain boundaries, the detectability probably is enhanced. This type of early-stage volumetric damage is possibly visualized as a blue haze and cloudy area around internal large microcracks and macrocracks or adjacent to the bar surface exposed to the hydrogen (Figure 4d, right). This surface of the bar is acting as a backwall for ultrasound and is represented by the solid red line in the front and side view images.

It was validated that the 10 MHz FMC/TFM LL path technique can better detect and size synthetic HTHA damage oriented parallel to the ID when compared to the TT path technique and lower-frequency techniques.

#### Investigation of Samples Removed from Service

In the third investigation step, the capabilities of PAUT sectorial scanning and FMC/TFM/ATFM (with LL and TT paths) techniques were assessed using samples removed from service with real, localized, and complex HTHA damage at different stages and morphology.

**Channel welds:** Potential HTHA blistering, micro-, and macrocracking indications were detected in the channel welds using a 10 MHz linear probe with the FMC/TFM TT technique. Multiple indications were detected in the HAZ of the most susceptible section of the shell-to-head circumferential weld. The ROI width was extended to cover the HAZ of the weld at the head side. Similar micro and macro indications were observed on the head side, but the severity was lower compared to the shell side. The analysis results for indication 2 are shown in the split screen views of Figure 6a. The B-scan image (Figure 6a, top left) analysis displays a root crack 5 mm high representing 34% wall thickness damage. The intersections of the vertical and horizontal cursors on the C-scan (Figure 6a, bottom left), cumulative D-scan (Figure 6a, bottom right), and D-scan single plane (Figure 6a, top right) show the location of the same crack-like indication. The elongated red areas on the right side of the C-scan and D-scans represent potentially breaking macrocracking at the root. The clusters of blue dots in the single-plane D-scan represent an early stage of HTHA damage. Indications of potential facets of HTHA damage were detected at skew  $-10^\circ$  in the breaking areas using the matrix probe and S-scan (Figure 6b). The matrix probe results in the second focalization plane indicate that the root crack is potentially continuous.

The metallographic investigation verified the presence of root cracking, stepwise cracking, and blistering with cracking edges. A cross-sectional image of the root crack is shown in Figure 7a. Optical metallography confirmed the matrix probe findings, showing that the crack in the HAZ is a continuous macrocrack along the weld starting from indication 2 and



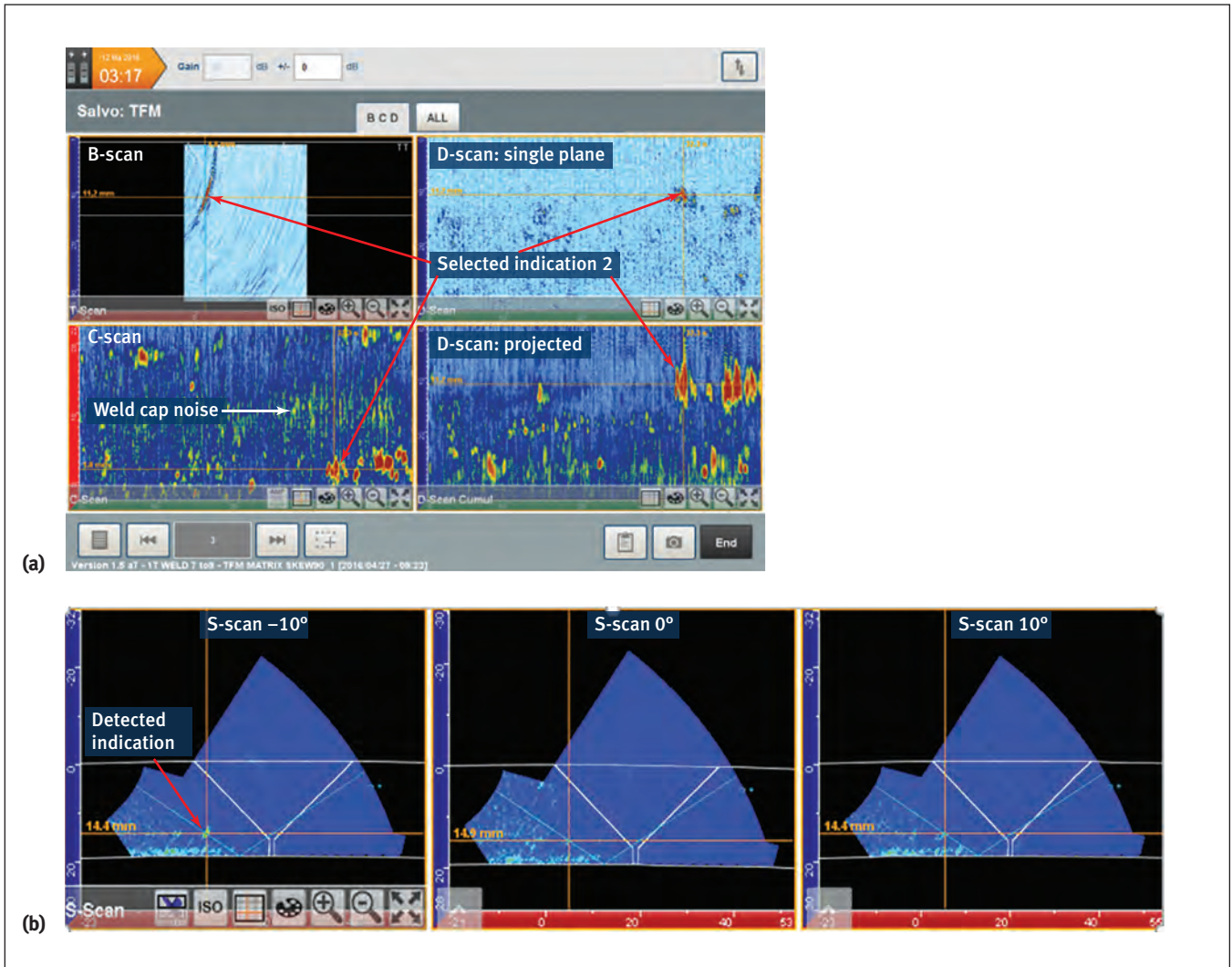


Figure 6. Imaging of HTHA weld damage using 10 MHz TT FMC/TFM and PAUT techniques: (a) linear probe split screen views of indication 2; (b) indication of potential HTHA damage detected in the breaking areas using matrix probe and S-scan at skew  $-10^\circ$ .

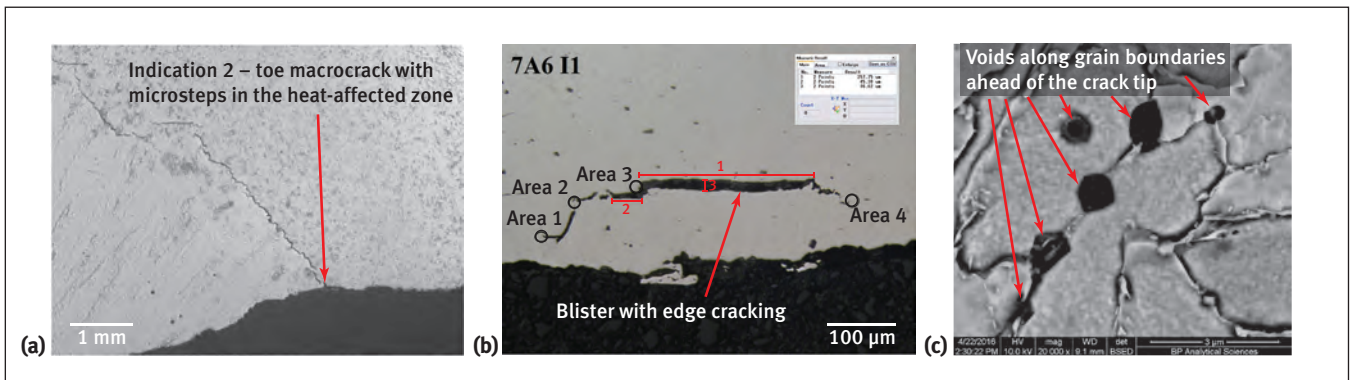


Figure 7. Weld damage validation using optical metallography and SEM: (a) root cracking in the heat-affected zone indicative of HTHA damage ( $\sim 20\times$ , nital etched); (b) blister with edge cracking ( $\sim 40\times$ , nital etched); (c) voids along grain boundaries ahead of the crack tip ( $\sim 20\,000\times$ , nital etched).

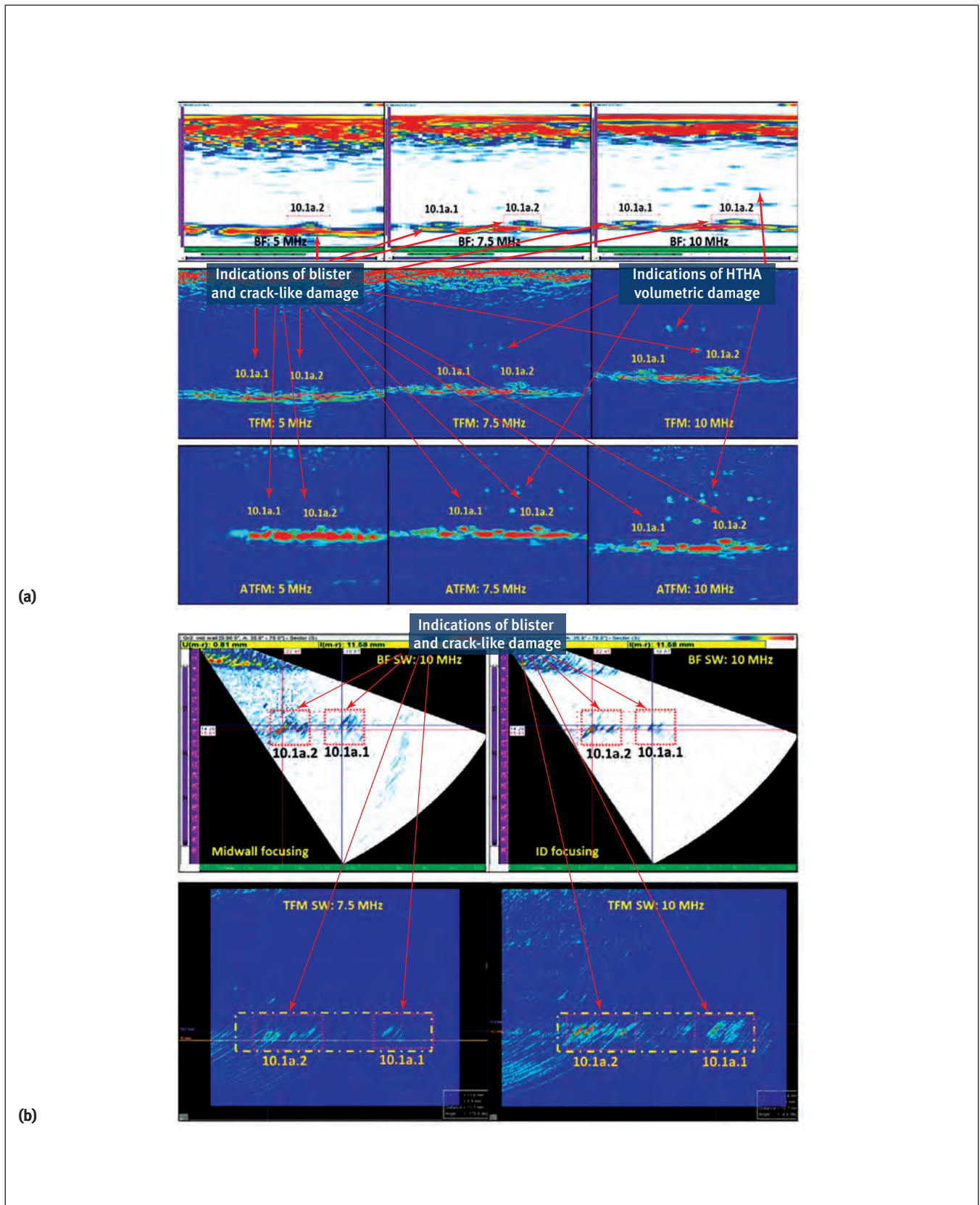


Figure 8. Imaging of indication 10.1a.1 and 10.1a.2: (a) PAUT straight-beam and FMC/TFM/ATFM LL B-scans comparison; (b) comparison of PAUT S-scans and FMC/TFM TT B-scans using shear wave techniques.

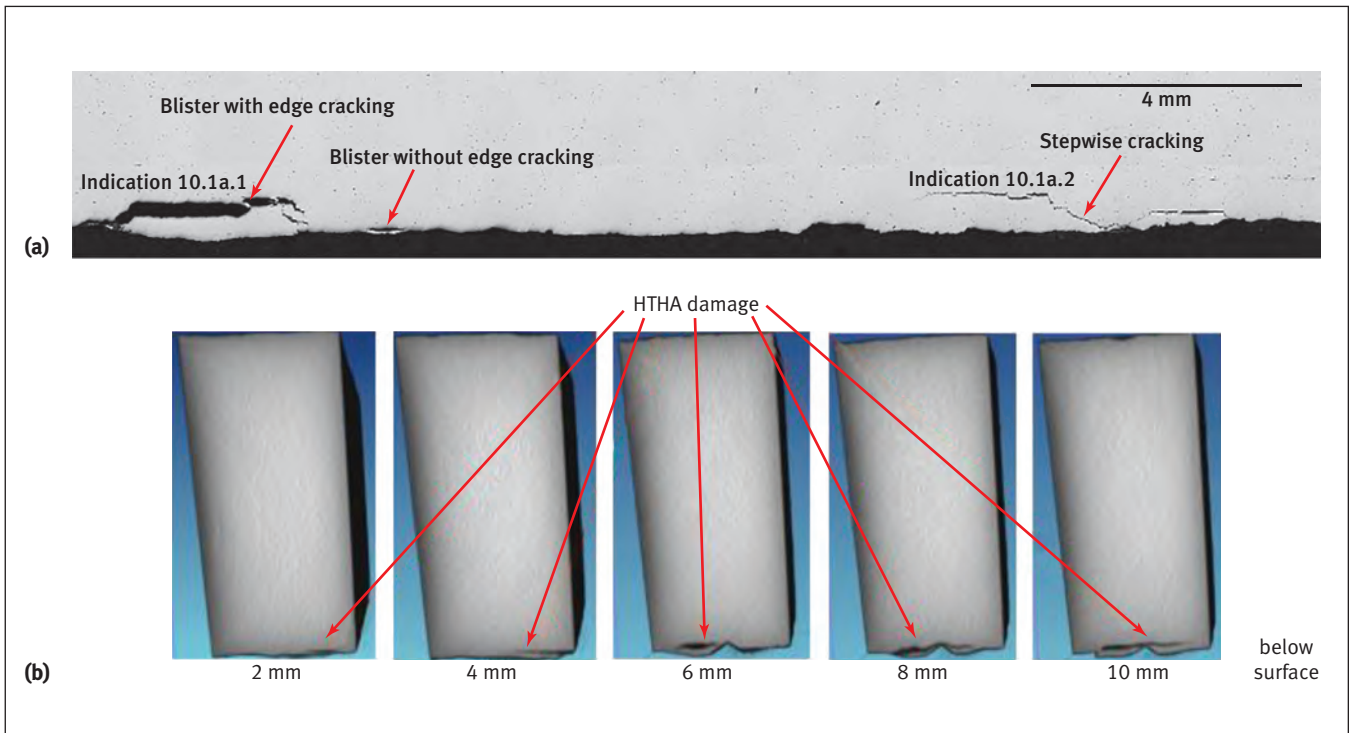


Figure 9. Metallographic and CT images: (a) indications 10.1a.1 and 10.1a.2,  $\sim 10\times$ , as polished; (b) CT images of indication 10.1a.2 from 2 to 10 mm below the polished surface of the mount.

finishing at the end of the scan. Macro stepwise cracking was observed in the base material adjacent to the root crack. Microscopic and macro blistering with cracking edges was documented near the ID (Figure 7b). Voids and linked voids, an indication of volumetric HTHA damage, were observed at the tips of the cracks and blisters at a higher magnification (Figure 7c). Single submicron voids and submicron linking voids were not detected with any array techniques. Stress-related microcracks were observed at the same magnification, but it was not possible to distinguish HTHA crack-like damage from stress-related microcracking with ultrasonic techniques.

**Channel base material:** A very small number of indications for a potential damage in the channel base material were identified on the 5 MHz C-scan in comparison to the relatively higher number of indications on the 7.5 and 10 MHz C-scans. Two indications (10.1a.1 and 10.1a.2) were selected for detailed analysis and comparison using projected or single-plane B-scans. Figure 8a illustrates the comparison of the single plane B-scans. The top row shows the PAUT (BF) B-scan, the middle row shows the FMC/TFM, and the bottom row shows the FMC/ATFM imaging. The left column consists of the 5 MHz technique imaging, the middle column is the 7.5 MHz technique imaging, and the right column is the 10 MHz technique imaging. The best detection

and image resolution for indications 10.1a.1 and 10.1a.2 was achieved using the 10 MHz FMC/ATFM LL technique (see bottom right image of Figure 8a). A cluster of smaller and weaker indications were detected above both indications using the same technique. The 10 MHz PAUT SW, 7.5 MHz, and 10 MHz FMC/TFM TT techniques confirmed the presence of both indications. The PAUT S-scan images using two focal laws (groups) are shown in the top part of Figure 8b. The first group was focused on the midwall (top left) and the second group was focused at the bottom (top right). The bottom row of Figure 8b represents TFM technique images for both the 7.5 and 10 MHz transducers.

The metallographic images for both indications are shown in Figure 9a. The enhanced detection and visualization capabilities of FMC/TFM and ATFM techniques at a higher frequency were validated metallographically. Indication 10.1a.1 was classified as two microblisters and 10.1a.2 as a stepwise microcrack. The complexity of the blistering and crack-wise morphology in the mount remnants was validated using CT. CT images of indication 10.1a.2 from 2 to 10 mm below the front polished surface of the mount are shown in Figure 9b.

The height and the width of the indications were measured from the metallographic images. A comparison of PAUT techniques results (longitudinal straight beam and angle shear wave beam) with FMC/TFM LL, FMC/TFM TT, FMC/ATFM LL, and metallographic measurements for



**TABLE 4**  
Height and width measurements of indication 10.1a.1

Frequency of the transducer	PAUT/TFM /ATFM	Height				Width			
		H <sub>metallography</sub>	H <sub>BF/TFM</sub>	$\Delta H = H_{BF} - H_M$	$(\Delta H/H_M) \times 100$	W <sub>metallography</sub>	W <sub>BF/TFM</sub>	$\Delta W = W_{BF} - W_M$	$(\Delta W/W_M) \times 100$
		mm	mm	mm	%	mm	mm	mm	%
LW-7.5 MHz	PAUT	0.57	1.00	0.43	75	2.4	4.6	2.2	91
LW-10 MHz		0.57	0.90	0.33	58	2.4	4.2	1.8	83
LW-5 MHz	TFM	0.57	0.90	0.33	58	2.4	4.0	1.6	67
LW-7.5 MHz		0.57	0.80	0.23	40	2.4	3.8	1.4	58
LW-10 MHz		0.57	0.70	0.13	23	2.4	3.3	0.9	38
LW-5 MHz	ATFM	0.57	0.80	0.23	40	2.4	3.8	1.4	58
LW-7.5 MHz		0.57	0.70	0.13	23	2.4	3.6	1.2	50
LW-10 MHz		0.57	0.60	0.03	5	2.4	2.9	0.5	21
SW-10 MHz	PAUT	0.57	0.90	0.33	58	2.4	4.0	1.6	67
SW-7.5 MHz	TFM	0.57	0.80	0.23	40	2.4	3.6	1.2	50
SW-10 MHz		0.57	0.70	0.13	23	2.4	3.2	0.8	33

indication 10.1a.1 are shown in Table 4. A 10 × 10 mm ROI was used for the FMC/TFM/ATFM techniques. A postprocessing tool called segmentation was applied to improve characterization and reduce the sizing inaccuracy. Better sizing results were demonstrated using high-frequency FMC/TFM and FMC/ATFM techniques.

**Drum welds and base material:** No signs of HTHA damage in the drum was reported using AUBT and TOFD during inspections of selected at-risk areas. An area of scattered blistering, measuring approximately 0.5 × 0.5 m, was detected visually during internal inspections, described in the following paragraphs.

The drum was removed from service, and PAUT and FMC/TFM raster and line scans were completed in four shell locations (base material) and in two weld locations. No indications for crack-like HTHA damage were detected in the weld and HAZ. Metallography confirmed the FMC/TFM findings that no crack-like HTHA damage was present in the weld and HAZ.

The 10 MHz FMC/TFM LL C-scan data analysis revealed widely spread, multiple indications of HTHA damage in the base material. In the south section of the drum, the localized blister-like damage had occurred in the base material and HAZ on both sides of the welds. The localized nature of the HTHA damage in one area of the south section and through-wall distribution is shown in Figure 10. FMC/TFM raster C-scans, through-wall thickness imaging, and the analysis determined that predominantly HTHA

damage in plate S1 is confined in less than 50% wall thickness, and plate S2 is limited in less than 20% wall thickness. A 3D TFM visualization of the expected blister-like damage is shown in Figure 11. An example of optical metallographic verification of micro- and macroblistering is shown in Figure 12a. Figure 12b shows a SEM image of voids formation and coalescence along grain boundaries at an early stage.

A less severe level of HTHA damage detected only in the base material of the north drum section is shown in Figure 13. The damage appeared as a “hockey stick” on the FMC/TFM raster C-scan image. Ninety-five percent of the indications were very shallow and compacted in 5% through-wall thickness. No indications were observed in a depth larger than 20% wall thickness. Six sets of reference SDHs that were manufactured in the front side of the plate were visualized at the bottom of the TFM images. The TFM line scan imaging (B- and D-scans) of the damage and a blister-like indication (N2-7.1.2; depth of 5.4 mm and length of 33.5 mm) are shown in Figure 14. Blister sizing based on 2D TFM multiview imaging suggested 10% to 20% larger dimensions compared to measurements using a digital caliper. A picture of visually observed scattered blistering (depth 1 to 3 mm and length 2 to 12 mm) is shown in Figure 15a. Reported larger TFM dimensions are due to bulging complexity and sharp blistering edges that were not contributing to the bulge’s visual appearance but subsidizing TFM imaging. An example of blister manifestation with sharp crack-like edges is shown in Figure 15b.

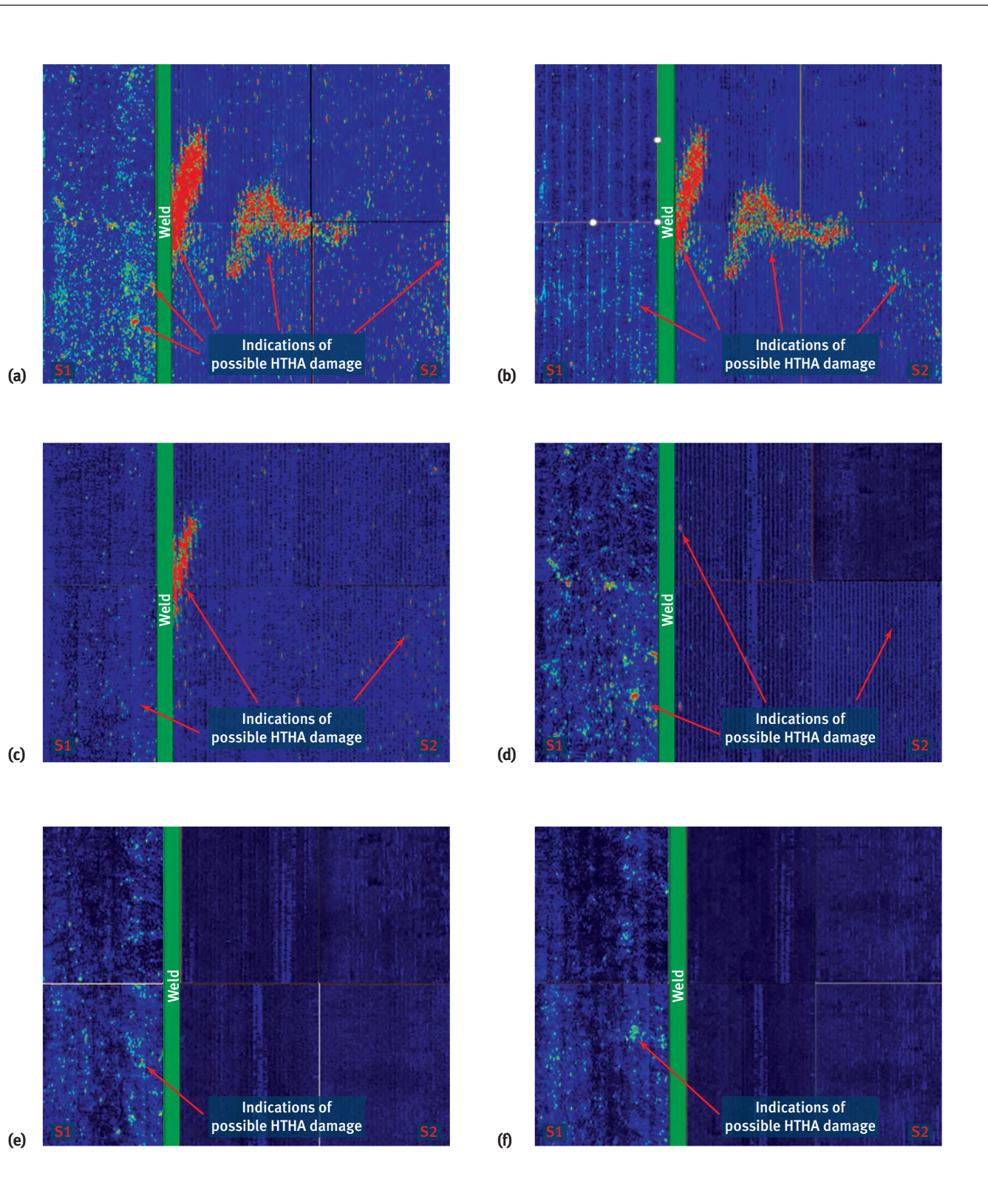


Figure 10. FMC/TFM imaging and HTHA validation of localized and through-wall distribution for the south section of drum: (a) 0% to 88% wall thickness (34 to 5 mm); (b) 0% to 5% wall thickness (34 to 32.3 mm); (c) 5% to 10% wall thickness (32.3 to 30.6 mm); (d) 10% to 20% wall thickness (30.6 to 27.2 mm); (e) 20% to 30% wall thickness (27.2 to 23.2 mm); (f) 30% to 50% wall thickness (23.2 to 17 mm).



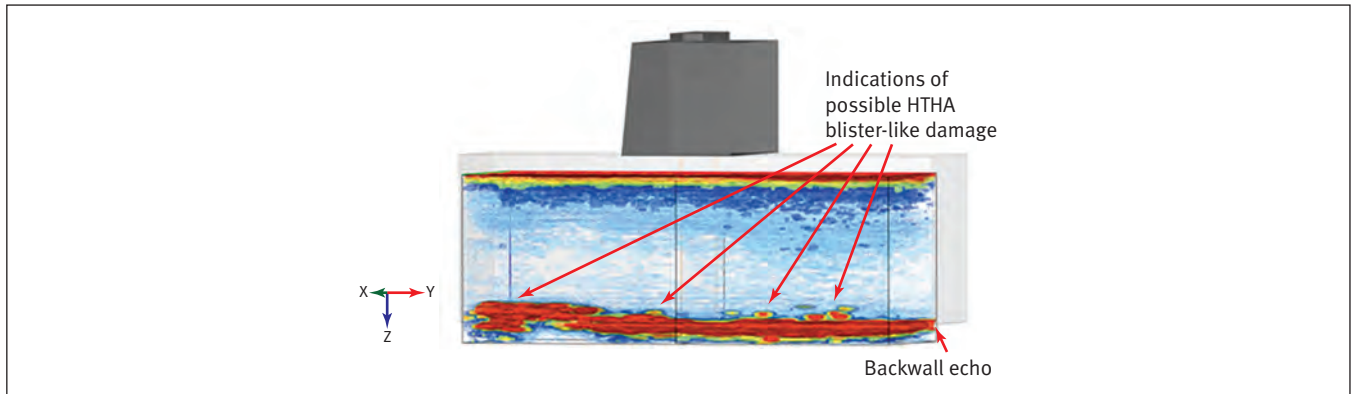


Figure 11. 3D imaging of possible blister-like damage.

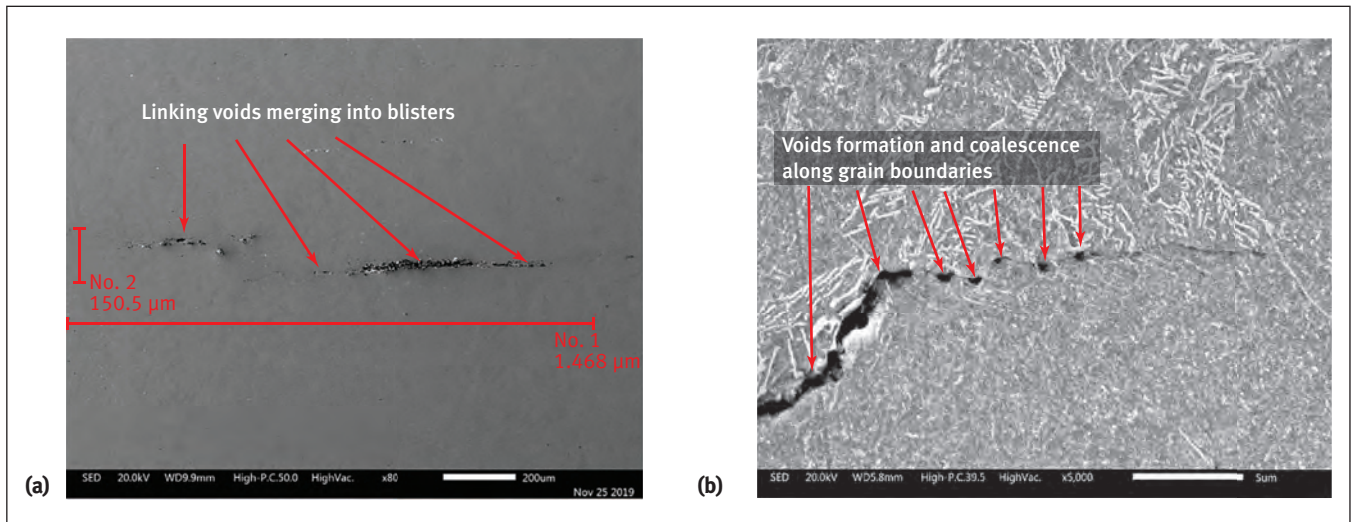


Figure 12. Optical metallography: (a) linking voids merging into blisters, ~80 $\times$ , as polished; (b) SEM validation of early-stage HTHA volumetric damage, ~5000 $\times$ , nital etched.

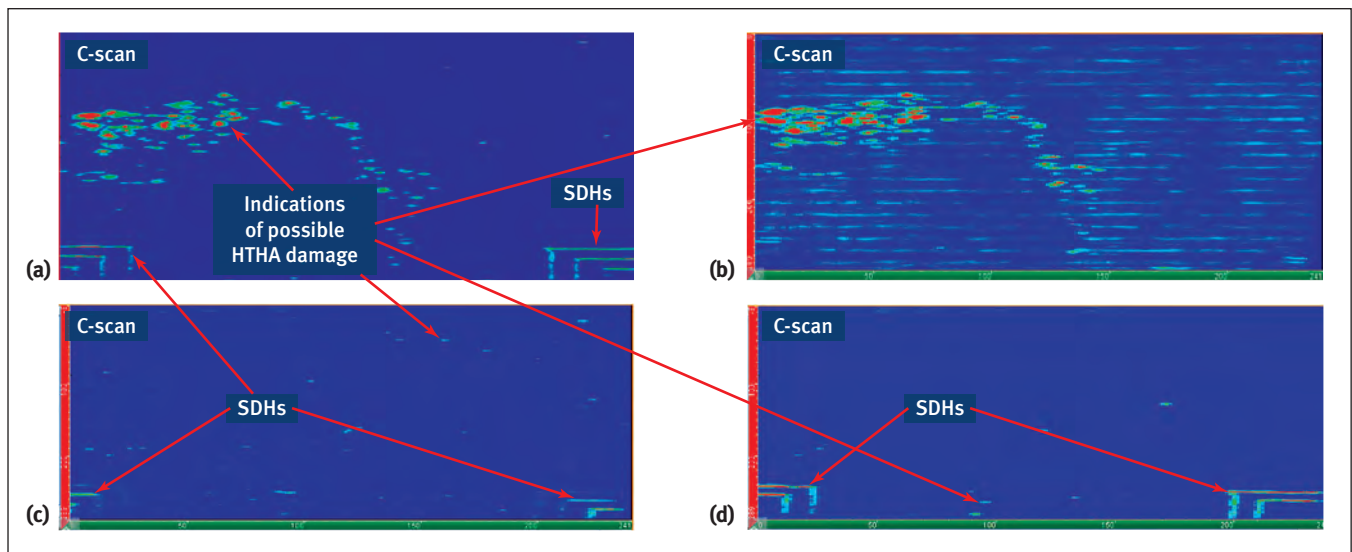


Figure 13. FMC/TFM imaging and HTHA validation raster C-scan imaging of possible HTHA damage localized and through-wall distribution for the north section of drum: (a) 0% to 70% wall thickness (34 to 10 mm); (b) 0% to 5% wall thickness (34 to 32.3 mm); (c) 5% to 10% wall thickness (32.3 to 30.6 mm); (d) 10% to 20% wall thickness (30.6 to 17 mm).



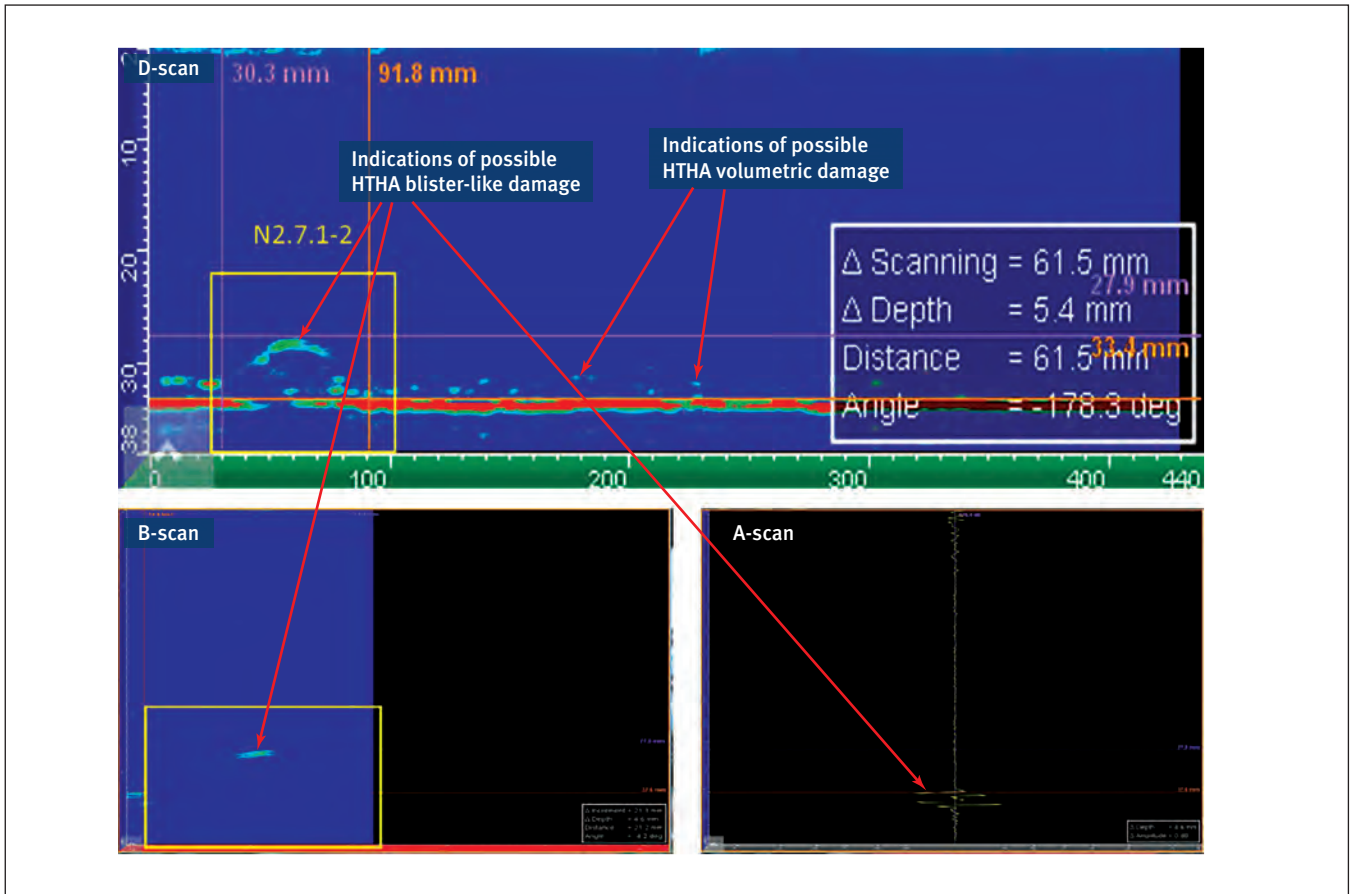


Figure 14. Line scan imaging of possible blistering with sharp crack-like edges.

The SEM photograph revealing the presence of nonmetallic inclusions and evidence of early-stage HTHA damage of void formation and voids coalescence associated with the inclusion location ahead of the blister edges is shown in Figure 15c.

It was validated that reliable detection, characterization, and sizing of in-service-induced, localized, and complex HTHA damage can be achieved when utilizing multiple FMC/TFM/ATFM with LL and TT paths and PAUT sectorial scan high-frequency techniques.

### Conclusions

This study has confirmed that optimized high-frequency FMC/TFM and FMC/ATFM techniques are more reliable and offer some advantages over PAUT and TOFD for HTHA inspection. These advantages include:

- better than 0.2 mm (200  $\mu\text{m}$ ) detection sensitivity for HTHA clustered volumetric damage, single blister, and crack-like indications and/or a combination of all of these;
- less sensitivity to the misorientation of the damage, since FMC records all reflected, backscattered, and diffracted signals, and the TFM image is created by summing multiple transmit–receive paths from all elements of the array;

- improved characterization as a result of enhanced spatial resolution such as the ability to resolve two or several closely spaced indications. When spaced apart larger than the grid ROI resolution, HTHA damage will be imaged better (without large arcs) and can be resolved;
- enhanced sizing resolution and more accurate sizing of HTHA clustered volumetric, blister, and crack-like indications because all points or pixels defined by the high-resolution grid within the ROI can be focused during the imaging process using TFM.

Applying more effective ultrasonic techniques for detection, characterization, and sizing HTHA in early stages could improve the confidence of fitness-for-service assessments. Damage growth could be monitored as a short-term mitigation strategy using frequent periodic inspections until the equipment is replaced.

Using FMC/TFM and FMC/ATFM as the primary techniques for more reliable early-stage HTHA inspection is recommended. PAUT is recommended as a backup for the primary techniques. TOFD is recommended only as a secondary and screening technique due to dead zones and characterization limitations.

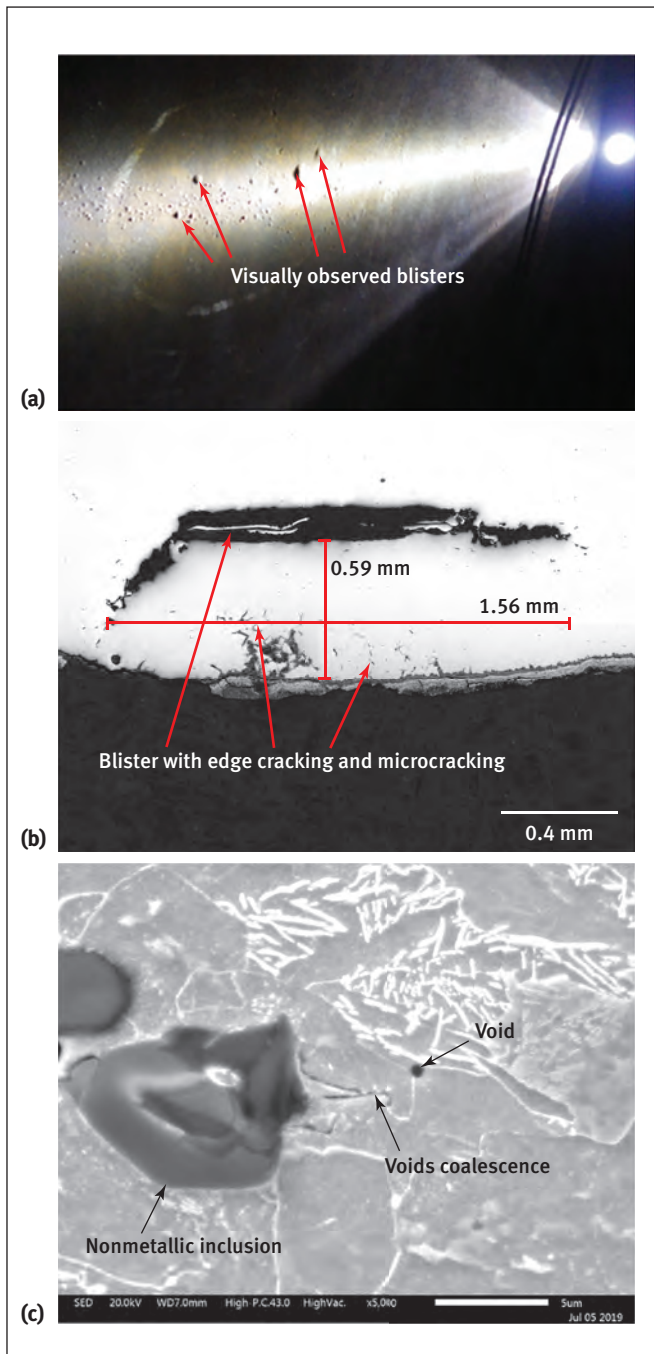


**Figure 15. Potential indications of HTHA: (a) visual validation of typical blister bulging; (b) optical metallography of blistering with sharp crack-like edges, ~50 $\times$ , as polished; (c) SEM of nonmetallic inclusions and evidence of early-stage HTHA damage of void formation and voids coalescence, ~5000 $\times$ , nital etched.**

#### ACKNOWLEDGMENTS

The authors acknowledge bp management for the permission to publish the paper and all coworkers for preliminary data collection, providing samples, and field support.

#### REFERENCES

- API, 2016, *API Recommended Practice 941: Steels for Hydrogen Service at Elevated Temperatures and Pressures in Petroleum Refineries and Petrochemical Plants*, 8th ed., American Petroleum Institute, Washington, DC.
- API, 2020, *API Recommended Practice 941: Steels for Hydrogen Service at Elevated Temperatures and Pressures in Petroleum Refineries and Petrochemical Plants*, 8th ed., Addendum 1, American Petroleum Institute, Washington, DC.
- ASME, 2019, *ASME Boiler and Pressure Vessels Code, Section V, Nondestructive Examination*, American Society of Mechanical Engineers, New York, NY.
- Birring, A.S., M. Riethmuller, and K. Kawano, 2005, "Ultrasonic Techniques for Detection of High Temperature Hydrogen Attack," *Materials Evaluation*, Vol. 63, No. 2, pp. 110–115.
- Calmon, P., F. Le Bourdais, X. Artusi, R. Miorelli, and S. Leberre, 2018, "Simulation-Based Performances Assessment of FMC-TFM Array Imaging Techniques," 12th European Conference on Non-Destructive Testing (ECNDT 2018), Gothenburg, Sweden.
- Holmes, C., B. Drinkwater, and P. Wilcox, 2004, "The Post-Processing of Ultrasonic Array Data Using the Total Focusing Method," *Insight*, Vol. 46, No. 11, pp. 677–680.
- Johnson, J., B. Olson, M. Swindeman, M. Carte, and J. Browning, 2019, "High Temperature Hydrogen Attack Life Assessment Modeling and Inspection," CORROSION 2019, Nashville, TN, Document ID: NACE-2019-13326.
- Kallenberg, G.P., and T. Munsterman, 2002, "Remaining Life Assessment of Catalytic Reforming Reactors," CORROSION 2002, Denver, CO, Document ID: NACE-02481.
- Krynicky, J.W., K.E. Bagnoli, and J.E. McLaughlin, 2006, "Probabilistic Risk Based Approach for Performing on Onstream High Temperature Hydrogen Attack Inspection," CORROSION 2006, San Diego, CA, Document ID: NACE-06580.
- Le Nevé, C., S. Loyan, L. Le Jeune, S. Mahaut, S. Demonte, D. Chauveau, R. Renaud, M. Tessier, N. Nourrit and A. Le Guellaut, 2019, "High Temperature Hydrogen Attack: New NDE Advanced Capabilities – Development and Feed Back," ASME 2019 Pressure Vessels and Piping Conference, San Antonio, TX.
- Lozev, M., L. Yu, P. Mammen, T.J. Eason, J. Chew, and G. Neau, 2017, "Phased Array Ultrasonic Techniques for Detection, Characterization and Sizing of High Temperature Hydrogen Attack," 2017 API Inspection Summit, Galveston, TX.
- Lozev, M.G., and R.L. Spencer, 2005, "Developing, Optimizing and Validating Automated Ultrasonic Procedures for Testing Heavy Walled Hydroprocessing Reactors," *Materials Evaluation*, Vol. 63, No. 9, pp. 926–932.
- McGovern, M.E., D.K. Balch, and H. Reis, 2017, "Non-destructive Evaluation and Characterisation of High-Temperature Hydrogen Attack in Carbon Steel Pressure Vessels," *Insight*, Vol. 59, No. 1, pp. 11–16.
- Nageswaran, C., 2018, "Maintaining the Integrity of Process Plant Susceptible to High Temperature Hydrogen Attack. Part 1: Analysis of Non-destructive Testing Techniques," Research Report RRI133, prepared by TWI Ltd. for the Health and Safety Executive, Cambridge, UK.
- Reverdy, F., L. Le Ber, O. Roy, and G. Benoist, 2018, "Real-Time Total Focusing Method on a Portable Unit, Applications to Hydrogen Damage and Other Industrial Cases," 12th European Conference on Non-Destructive Testing (ECNDT 2018), Gothenburg, Sweden.
- Robert, S., F. Cartier, L. de Roumilly, R.-O. Mondou, P.-E. Lhuillier, and G. Garzino, 2016, "Adaptive Ultrasonic Imaging with a Phased-Array Probe Equipped with a Water-Filled Conformable Wedge," 19th World Conference on Non-Destructive Testing (WCNDT 2016), Munich, Germany.
- Schmerr Jr., L.W., 2015, *Fundamentals of Ultrasonic Phased Arrays*, Springer.
- Wang, W.D., 1999, "Ultrasonic Detection, Characterization, and Quantification of Localized High Temperature Hydrogen Attack in Weld and Heat-Affected Zone," *In Service Experience in Fossil and Nuclear Power Plants* (ed. J. Pan), Vol. 392, American Society for Mechanical Engineers, New York, NY, pp. 291–298.
- Wilcox, P.D., 2013, "Ultrasonic Arrays in NDE: Beyond the B-scan," *AIP Conference Proceedings*, Vol. 1511, No. 1, pp. 33–50.